Nanoscale cellular organization of viral RNA and proteins in SARS-CoV-2 replication organelles

Leonid Andronov*[1], Mengting Han*[2], Yanyu Zhu[2], Anish R. Roy[1], Andrew E. S. Barentine[1], Jaishree Garhyan[3], Lei S. Qi[2,4,5], W.E. Moerner[1,4]

[1]Department of Chemistry; [2]Department of Bioengineering; [3]In Vitro Biosafety Level 3 (BSL-3) Service Center, School of Medicine; [4]Sarafan ChEM-H; Stanford University, Stanford, CA 94305 U.S.A. [5]Chan Zuckerberg Biohub – San Francisco, San Francisco, CA 94158 U.S.A.

*These authors contributed equally.

#Correspondence to: W. E. Moerner, wmoerner@stanford.edu; Lei S. Qi, sqi@stanford.edu

Abstract:

The SARS-CoV-2 viral infection transforms host cells and produces special organelles in many ways, and we focus on the replication organelle where the replication of viral genomic RNA (vgRNA) occurs. To date, the precise cellular localization of key RNA molecules and replication intermediates has been elusive in electron microscopy studies. We use super-resolution fluorescence microscopy and specific labeling to reveal the nanoscopic organization of replication organelles that contain vgRNA clusters along with viral double-stranded RNA (dsRNA) clusters and the replication enzyme, encapsulated by membranes derived from the host endoplasmic reticulum (ER). We show that the replication organelles are organized differently at early and late stages of infection. Surprisingly, vgRNA accumulates into distinct globular clusters in the cytoplasmic perinuclear region, which grow and accommodate more vgRNA molecules as infection time increases. The localization of ER labels and nsp3 (a component of the double-membrane vesicle, DMV) at the periphery of the vgRNA clusters suggests that replication organelles are enclosed by DMVs at early infection stages which then merge into vesicle packets as infection progresses. Precise co-imaging of the nanoscale cellular organization of vgRNA, dsRNA, and viral proteins in replication organelles of SARS-CoV-2 may inform therapeutic approaches that target viral replication and associated processes.

Keywords: SARS-CoV-2 coronavirus, viral replication, fluorescence imaging, super-resolution fluorescence microscopy, viral RNA localization, COVID-19, viral proteins, cell infection

Introduction

Due to its global health impact, the SARS-CoV-2 betacoronavirus and its infection of mammalian cells have been the subject of a large number of studies across multiple fields. Biochemical methods have allowed researchers to investigate the interactions between the viral oligonucleotides and the host proteins *in vitro* and in cellular extracts, leading to much insight[1,2]. There have also been electron microscopy (EM) studies of resin-embedded samples as well as vitrified samples using cryo-electron tomography, all of which have been profiting from the large increase in EM resolution and contrast in recent years. These EM studies can provide very high-resolution structures of protein complexes as well as tomograms of organelles in the cellular context. High-contrast filamentous structures and membranes appear regularly in such images, allowing identification of single- and double-membrane vesicles (DMVs)[3-5]. However, the all-important viral RNA and associated proteins are challenging to identify by EM due to a lack of specific contrast. While some researchers have detected RNA-like filaments in vesicles[4,5], further investigations are needed to identify specific viral RNAs in the cellular context.

Fluorescence microscopy offers a highly useful and complementary set of capabilities, most importantly the specific labeling of proteins or RNA sequences. However, conventional diffraction-limited (DL) fluorescence microscopy, with its resolution constrained to ~250 nm, is unable to resolve the tiny structures that are hidden in a blurred DL image. Super-resolution (SR) microscopy based on single molecules (PALM[6], (d)STORM[7,8]) or on structured patterns of molecular depletion (STED[9], SIM[10]), however, offers far better optical resolution down to 10 nm and below. A wealth of important cellular patterns and structures have been identified in recent years, such as the banding patterns of axonal proteins in neuronal cells[11] and many others[12-14]. The specificity of SR imaging is useful to apply to the study of viral genomic RNA (vgRNA) and other RNA molecules; moreover, additional imaging of critical protein players involved in coronavirus infection of cells provides crucial context for the nearby partners and surroundings of the viral RNA. In a previous proof-of-principle study, we explored the relatively safe human coronavirus 229E (HCoV-229E) from the alphacoronavirus family, which uses the APN receptor and produces only mild cold symptoms[15].

77 In this work, we apply multicolor confocal microscopy and SR microscopy to explore the
78 localization patterns of viral RNA and protein molecules for SARS-CoV-2 betacoronavirus during
79 the early and late infection of mammalian cells. We focus particularly on viral genomic RNA
80 (vgRNA) and its relative, the double-stranded RNA (dsRNA) that forms between the (+) sense
81 vgRNA and the (-) sense copy. After the initial infection with a few copies of vgRNA, more vgRNA
82 and dsRNA are synthesized by the RNA-dependent RNA polymerase complex (RdRp), an early
83 essential enzyme formed by ribosomal polyprotein synthesis and the viral proteases. We also co-
84 image a series of molecules, including membrane markers, nucleocapsid protein, spike protein,
85 and the nsp3 protein (reported to be a major component of a molecular pore spanning both
86 membranes of DMVs[16]), all to provide context and support for the view that vgRNA, dsRNA, and
87 RdRp act spatially in replication organelles (ROs) during virus replication. Thus, we provide key
88 information about where these important players are found in infected cells and how they change
89 with time during infection. Our results yield a nanoscale optical readout of viral nucleic acid
90 organization during SARS-CoV-2 infection, highlight the structural importance of ROs, and could
91 potentially benefit development of future therapeutic approaches.

92

93 **Results**

94 *Labeling and imaging of SARS-CoV-2 virions*

95 To specifically detect SARS-CoV-2 vgRNA, we applied RNA fluorescence *in situ* hybridization (RNA
96 FISH) with 48 antisense DNA oligonucleotide probes[17] specifically targeting the open reading
97 frame 1a (ORF1a) region which is only present in vgRNA and not in subgenomic RNAs (sgRNAs),
98 ensuring detection of only full-length viral (+)vgRNA (Fig. 1a). Each probe was conjugated with a
99 single blinking fluorophore for (d)STORM (direct Stochastic Optical Reconstruction Microscopy)[8].
100 To test this labelling and imaging approach, we first imaged vgRNA along with SARS-CoV-2 spike
101 protein in purified virions (Supplementary Fig. S1). While the size of SARS-CoV-2 virions is too
102 small to resolve in conventional DL fluorescence microscopy (Supplementary Fig. S1a), in SR the
103 internal concentric organization of the virions can be observed with vgRNA found in their center
104 and spike at the surface (Supplementary Fig. S1b). The labelling efficiency with these probes is

105 around 6 dyes/vgRNA in partially Proteinase K-digested virions, which was higher than in intact
106 virions due to poorer accessibility of their vgRNA (Supplementary Fig. S1c-i).

107 Next, we imaged SARS-CoV-2 infected Vero E6 cells that were fixed at 24 hours post infection (hpi)
108 and then labeled for immunofluorescence imaging (Methods). Spike and nucleocapsid SR
109 microscopy in these cells revealed assembled virions mostly at the cellular periphery, often at
110 cytoplasmic tubular projections, indicating active viral production (Supplementary Fig. S1j),
111 similar to previously reported results[5,18]. We now turn to the main focus of this study, the
112 replication of viral genomic RNA.

113

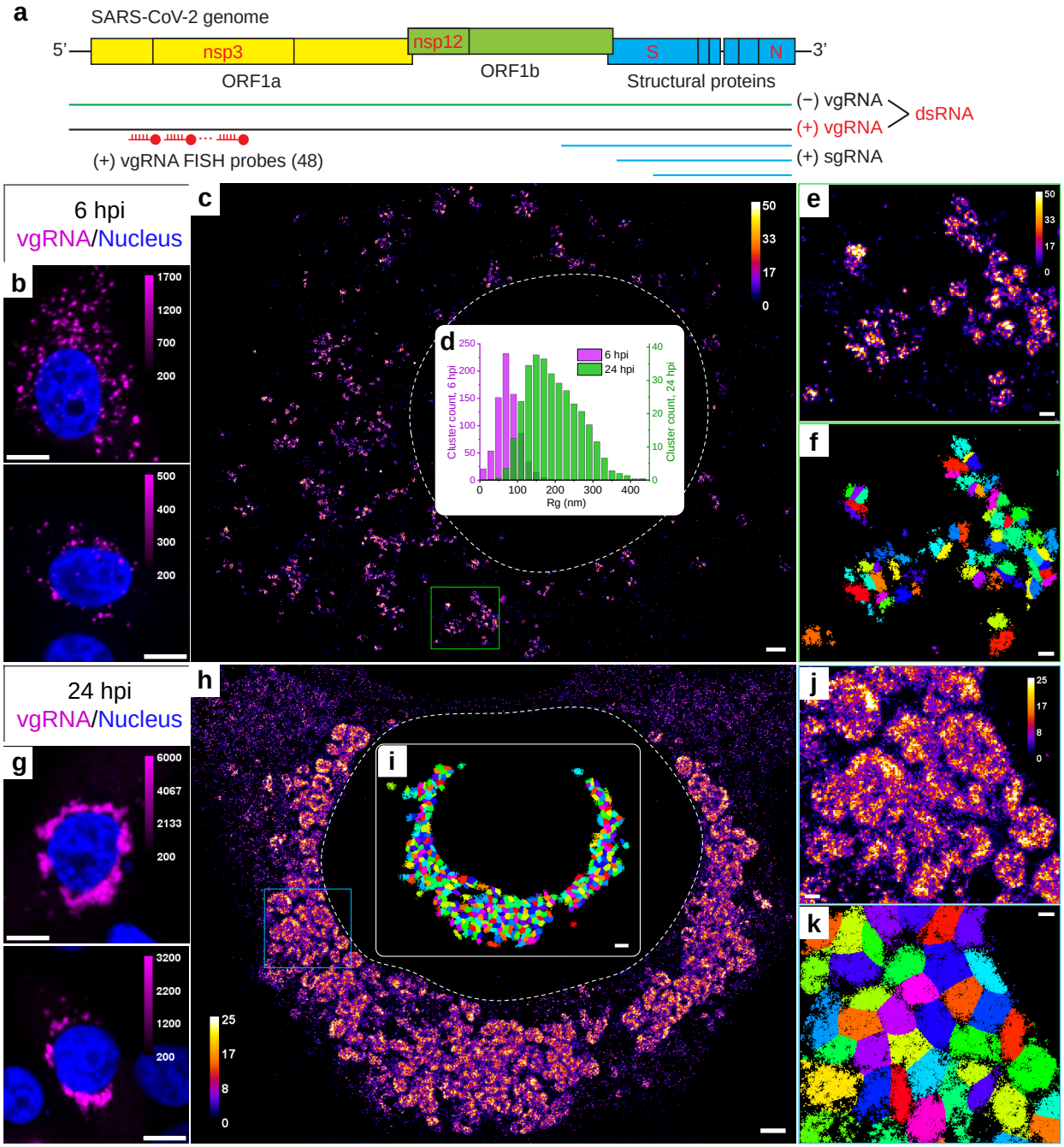

Fig. 1: Clustering of vgRNA in the cytoplasm of infected cells.

a, Scheme of SARS-CoV-2 genome with constructs used for its detection in infected cells. 48 antisense DNA oligonucleotide probes were used to target the ORF1a-coding region of vgRNA that is exclusive to the (+)vgRNA and does not occur in the sgRNAs. The RNA FISH probes are conjugated with AF647 or CF568. **b**, Representative confocal images of vgRNA in infected Vero E6 cells at 6 hpi display scattered DL puncta. **c**, Representative SR image of an infected cell at 6 hpi reveals distinct vgRNA clusters in the cytoplasm. **d**, Histogram of the radii of gyration (Rg) of the

vgRNA clusters indicate their size increase between 6 hpi (magenta) and 24 hpi (green). **e**, Zoomed-in region of the SR image (green frame in **c**) displays an agglomeration of vgRNA clusters. **f**, BIC-GMM cluster analysis of the region shown in **e**. **g**, Representative confocal images of vgRNA in infected Vero E6 cells at 24 hpi display large DL foci in the perinuclear region of the cytoplasm. **h**, Representative SR image of an infected cell at 24 hpi reveals large perinuclear vgRNA clusters. **i**, BIC-GMM cluster analysis of the cell shown in **h**. **j**, Zoomed-in region of the SR image (blue frame in **h**) displays dense vgRNA clusters. **k**, BIC-GMM cluster analysis of the region shown in **j**. Scale bars, 10 µm (**b**, **g**), 1 µm (**c**, **h**, **i**), 200 nm (**e**, **f**, **j**, **k**). Dashed lines in **c** and **h** indicate the position of the cell nucleus. Localizations that belong to the same cluster in **f**, **i**, **k** are depicted with the same color. Color bars in **c**, **e**, **h**, **j** show the number of SM localizations within each SR pixel (20 x 20 nm^2).

SARS-CoV-2 genomic RNA clusters in cytoplasm of infected cells

Confocal screening demonstrated three patterns of intracellular vgRNA localization (Supplementary Fig. S2a): scattered puncta in the cytoplasm (Type 1, Fig. 1b), appearance of bright foci in the perinuclear region (Type 2, Supplementary Fig. S2a), and concentration of vgRNA into large dense structures that occupy most of the perinuclear region (Type 3, Fig. 1g). We find that Type 1 cells were most abundant at 6 hpi, and Type 3 cells at 24 hpi, indicating that the vgRNA localization progresses from Type 1 to Type 3 as infection advances in time (Supplementary Fig. S2b). We also find that the cell-integrated vgRNA FISH signal in infected cells increases 2.2x on average from 6 to 24 hpi (Supplementary Fig. S2c), representing active viral replication and accumulation of vgRNA inside the cells.

The higher spatial resolution of SR microscopy revealed that at 6 hpi (Type 1 and Type 2 cells), most vgRNA localizes into clusters with an approximately round shape and a diameter of 100-250 nm that scatter in the cytoplasm (Fig. 1c, e). At 24 hpi (Type 2 and Type 3 cells), the vgRNA localization pattern transformed into a fascinating dense perinuclear network of approximately round, often hollow structures with a diameter of 300-700 nm (Fig. 1h, j). To quantify the transformation of vgRNA clusters in infected cells, we performed a Bayesian Information Criterion-optimized Gaussian Mixture Model clustering analysis (BIC-GMM) (Fig. 1f, i, k; See

152 Methods). This analysis showed an increase in the median vgRNA cluster size (radius of gyration)
153 from 73 nm at 6 hpi to 187 nm at 24 hpi (Fig. 1d, see inset) reflecting the drastic change in vgRNA
154 localization pattern.

155 Besides dense vgRNA clusters, we observe isolated localizations of individual vgRNA molecules
156 scattered in the cytoplasm at both time points, in line with previously reported results[15,17]. These
157 appear as a haze in confocal images (Supplementary Fig. S2a, Type 3) but are resolved as sparse
158 nanoscale puncta (d < 50 nm) in SR (Fig. 1h, Supplementary Fig. S3a) which we assume to be
159 single vgRNA copies (even though the puncta are more dense at 24 hpi). Using the average
160 number of single-molecule (SM) localizations per vgRNA punctum as a calibration for the number
161 of localizations per single vgRNA, we estimated the average number of vgRNA molecules in the
162 vgRNA clusters to be around 26 vgRNA/cluster at 6 hpi, increasing by almost an order of
163 magnitude to 181 vgRNA/cluster at 24 hpi (Supplementary Fig. S3b-c).

164

165 *dsRNA associates with vgRNA clusters*

166 Next, we proceeded to assess the relation of vgRNA cluster locations to viral replication. For this,
167 we immunofluorescently labelled an intermediate of coronavirus replication and transcription,
168 the hybridized dsRNA objects composed of (+) sense vgRNA and (-) sense copy, and co-imaged
169 dsRNA with vgRNA using two-color confocal and SR microscopy. These targets appeared mostly
170 colocalized at both time points at low resolution (Fig. 2a-b), suggesting that vgRNA clusters are
171 often found close to the replication centers of SARS-CoV-2. SR microscopy revealed that dsRNA
172 aggregates into clusters of a relatively compact size (d ≈ 100-200 nm) with distinct patterns of
173 colocalization with vgRNA at 6 or 24 hpi (Fig. 2c-e).

174 To quantify the spatial relationship between dsRNA and vgRNA, we conducted pair-pair
175 correlation analysis[19]. We calculated a bivariate pair-correlation function $g_{12}(r)$, *i.e.*, the
176 distribution of the pairwise distances between the localizations of the two species[20]. The function
177 is computed only in perinuclear regions and is normalized in a way that $g_{12}(r) = 1$ for two randomly
178 and homogeneously distributed species, signifying complete spatial randomness (CSR). Closely
179 associated or colocalized species have a prevalence of short pairwise distances resulting in a peak

180 in $g_{12}(r)$ near $r = 0$, while anti-correlated species lack short interparticle distances, which lowers
181 $g_{12}(r)$ at $r = 0$ followed by peaking at $r > 0$.

182 At early infection stages (6 hpi), dsRNA clusters appear closely associated with or adjacent to
183 vgRNA clusters both visually and by pair-pair correlation analysis (Fig. 2c, f). By contrast, during
184 late infection (24 hpi), dsRNA clusters anticorrelate with vgRNA at short distance scales with an
185 average separation between them around 120 nm as indicated by bivariate pair-correlation
186 functions $g_{12}(r)$ (Fig. 2g). Moreover, at 24 hpi, dsRNA clusters can often be found in the voids of
187 the large vgRNA structures (Fig. 2d), suggesting their possible concentric localization in the same
188 ROs.

189 Contrary to vgRNA, the size of dsRNA clusters slightly decreases and the total brightness of
190 cellular dsRNA labelling does not significantly change between 6 hpi and 24 hpi (Fig. 2e,
191 Supplementary Fig. S2d). Interestingly, at 6 hpi but not at 24 hpi, the dsRNA signal per cell
192 positively correlates with that of vgRNA signal (Supplementary Fig. S2f-g). These findings indicate
193 that the amount of dsRNA increases at early infection but reaches saturation by 24 hpi. This may
194 suggest that after the rapid initial production of a dsRNA pool, further generation of (-) sense
195 copies slows down and the replication shifts to the generation of vgRNA from the pool of available
196 (-) sense copy templates, which is common in other coronaviruses[21].

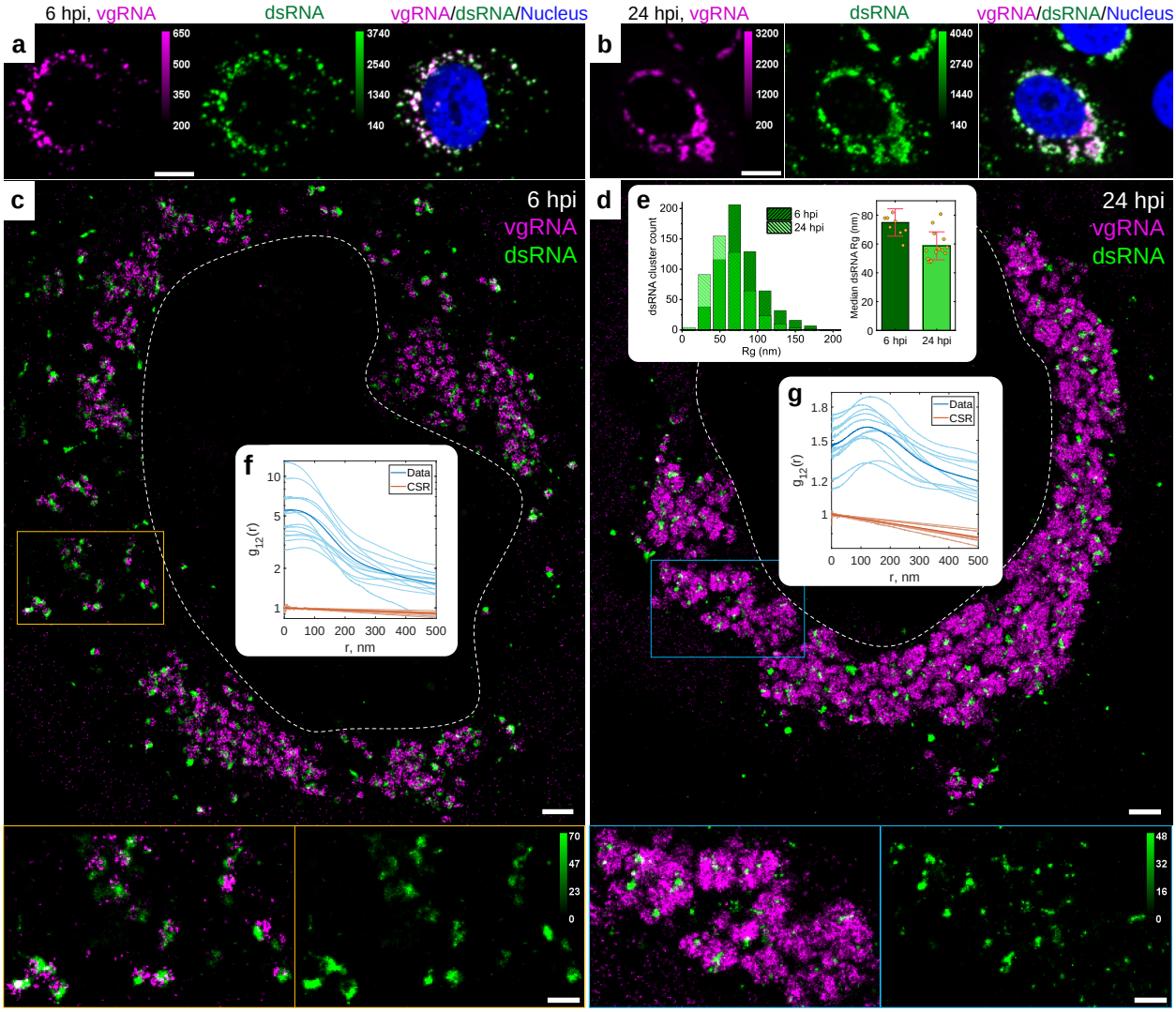

Fig. 2: Association of dsRNA with vgRNA clusters

a-**b**, Representative confocal images of SARS-CoV-2 infected cells display DL colocalization between dsRNA (green) and vgRNA (magenta) at both 6 hpi (**a**) and 24 hpi (**b**). **c**-**d**, Representative SR images of SARS-CoV-2 infected cells indicate association between dsRNA and vgRNA at 6 hpi (**c**) and short-range anti-correlation often with concentric localization at 24 hpi (**d**). Bottom panels, zoomed-in images of corresponding colored boxes. **e**, Histogram of Rg of dsRNA clusters as determined by the BIC-GMM cluster analysis (left). Median Rg of dsRNA clusters significantly decreases between 6 hpi and 24 hpi (right). p-value = $8 \cdot 10^{-4}$, two-tailed t-test. (**f**-**g**), Bivariate pair-correlation functions $g_{12}(r)$ calculated between the localizations of dsRNA and vgRNA indicate close association at 6 hpi (**f**) and nanoscale anti-correlation at 24 hpi (**g**). CSR, complete spatial randomness. Thin lines correspond to $g_{12}(r)$ of individual cells and bold lines are the mean values of $g_{12}(r)$ from all analyzed cells. Scale bars, 10 µm (**a**-**b**), 1 µm (**c**-**d**), 500 nm (**c**-**d**, bottom panels). Dashed lines in **c** and **d** indicate the position of the cell nucleus.

211 *vgRNA clusters denote the replication centers of SARS-CoV-2 genome*

212 To investigate SARS-CoV-2 replication activity at the vgRNA clusters in more detail, we co-imaged
213 them with the RdRp complex, the replicating SARS-CoV-2 RNA-dependent RNA polymerase[22,23],
214 using immunofluorescent labelling of its catalytic subunit nsp12[24]. In confocal images, nsp12
215 adopts a similar pattern as vgRNA, colocalizing with it at both 6 hpi and 24 hpi (Fig. 3a-b), which
216 suggests ongoing replication at the vgRNA clusters. In SR images, nsp12 localized in small sparse
217 puncta (d < 50 nm) that were scattered within and next to the vgRNA clusters at both time points
218 (Fig. 3c-d). Because nsp12 puncta are well separated from each other, and oligomerization is not
219 expected[22,23,25], each nanoscale punctum is likely to represent a single replicating enzyme. On
220 average, we detected 2.5 nsp12 puncta per vgRNA cluster at 6 hpi and 7.6 at 24 hpi (Fig. 3g).

221 Interestingly, in contrast to vgRNA but similar to dsRNA, the total cellular amount of nsp12 does
222 not significantly increase (Supplementary Fig. S2e) and its nanoscale localization pattern stays the
223 same as infection progresses from 6 to 24 hpi (Fig. 3c-d). This suggests that the growth of vgRNA
224 clusters arises from a relatively constant small number of replication components between 6 and
225 24 hpi highlighted by the constant amount of dsRNA and RdRp. Bivariate cross-correlation
226 functions calculated between nsp12 and vgRNA localizations peaked at 0 nm indicating
227 association of these two targets at both 6 and 24 hpi (Fig. 3e-f). Since vgRNA clusters colocalize
228 with the catalytic subunit of RdRp, we conclude that vgRNA clusters combined with the nearby
229 RdRp enzymes and dsRNA highlight ROs that act as centers for replication and transcription of
230 SARS-CoV-2.

231

232

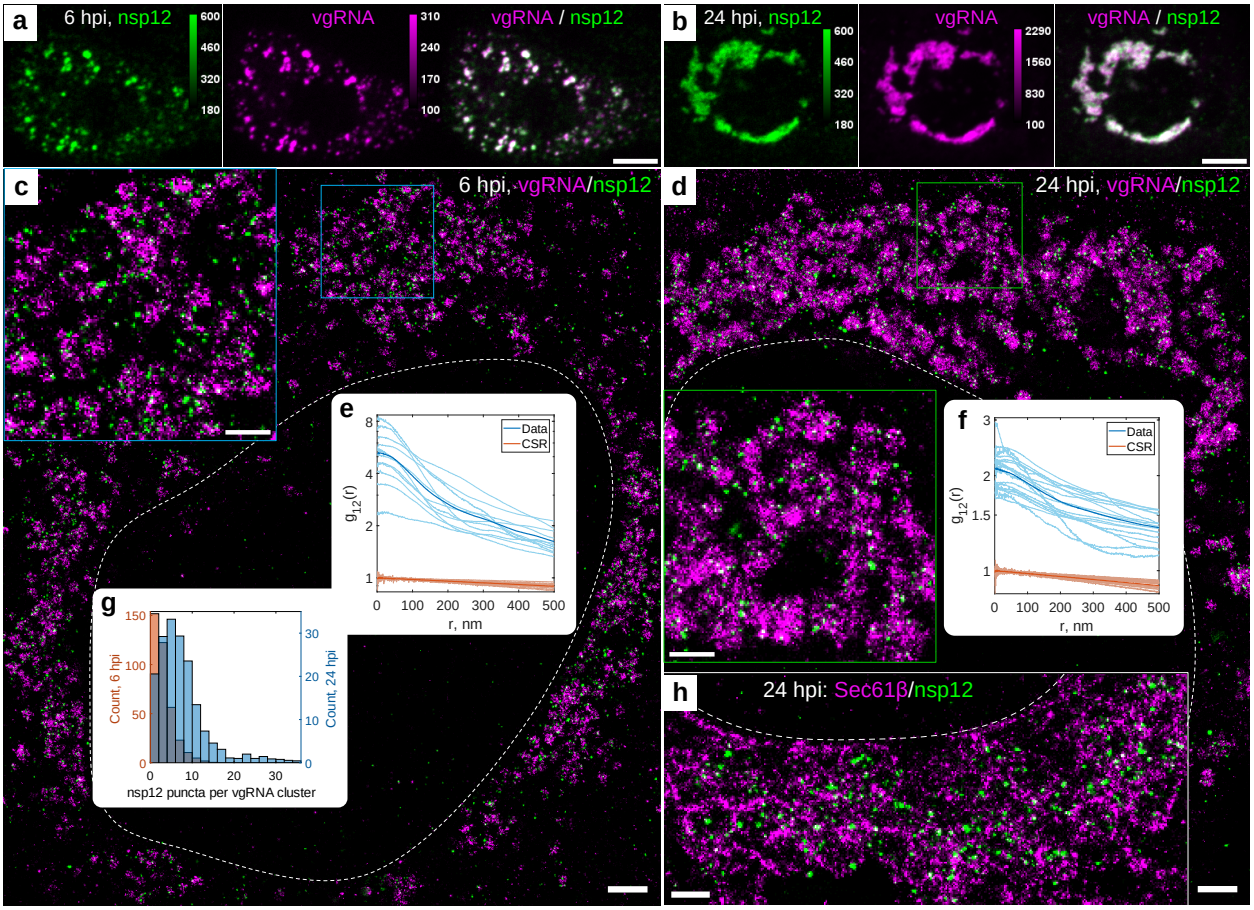

Fig. 3: Association of SARS-CoV-2 replication enzyme with vgRNA clusters

a-**b**, Representative confocal images of SARS-CoV-2 infected cells display DL colocalization between nsp12, the catalytic subunit of RdRp (green) and vgRNA (magenta) at both 6 hpi (**a**) and 24 hpi (**b**). **c**-**d**, Representative SR images of SARS-CoV-2 infected cells indicate nanoscale association between nsp12 and vgRNA at both 6 hpi (**c**) and 24 hpi (**d**). Insets show magnified images of corresponding regions in colored boxes. **e**-**f**, Bivariate pair-correlation functions peak at r = 0 nm indicating association between nsp12 and vgRNA at both 6 hpi (**e**) and 24 hpi (**f**). **g**, Number of nanoscale puncta of nsp12 per vgRNA cluster. **h**, SR image of nsp12 with Sec61β suggests encapsulation of nsp12 within ER-derived membranes. Scale bars, 10 µm (**a**-**b**), 1 µm (**c**-**d**), 500 nm (**h** and insets in **c**-**d**). Dashed lines in **c**, **d** and **h** indicate the edge of the cell nucleus.

vgRNA clusters are enclosed in ER-derived membranous organelles

Coronaviruses are thought to transform the host ER into replication-permissive structures, such as convoluted membranes and DMVs[3,26,27]. To investigate the relation of vgRNA clusters with cellular ER, we immunofluorescently labelled Sec61β, an ER membrane protein[28], in Vero E6 cells

249 stably expressing Sec61β-GFP[15]. Confocal images of these cells show the appearance of Sec61β
250 spots that colocalize with vgRNA against the mostly unaltered ER background at 6 hpi (Fig. 4a). At
251 24 hpi, however, substantial amounts of Sec61β accumulate close to the perinuclear vgRNA
252 clusters, while the ER tubules outside these regions become poorly visible (Fig. 4a), consistent
253 with the virus-induced rearrangement of the ER and the inhibition of host gene expression by
254 SARS-CoV-2[29].

255 In SR, we observe encapsulation of the vgRNA clusters by ring-like structures of the altered ER at
256 6 hpi (Fig. 4b, Supplementary Fig. S4). As infection progresses, the ER-derived ring- or sphere-like
257 structures grow to accommodate larger vgRNA clusters at 24 hpi (Fig. 4b, Supplementary Fig. S5).
258 Pair-correlation functions peak at the distance of the typical radius of vgRNA clusters indicating
259 nanoscale anti-correlation compatible with the ER-derived encapsulation of vgRNA (Fig. 4c).
260 dsRNA (Fig. 4b, Supplementary Fig. S6) and nsp12 (Fig. 3h) are also found to be encapsulated by
261 the same remodeled ER membranes suggesting that vgRNA, dsRNA and RdRp are all located
262 within the same ER-derived ROs.

263 To further confirm that these clusters are surrounded by membranes, we used a (d)STORM-
264 compatible general membrane marker CellMask Deep Red[30]. This dye broadly stains cellular
265 membranes, including the nuclear envelope, mitochondrial membranes, and SARS-CoV-2 virions
266 at the plasma membrane (Supplementary Fig. S7). The nanoscale image contrast with CellMask
267 Deep Red is poorer than specific protein labelling of the Sec61β ER label due to background from
268 membranes of different cellular organelles. Nevertheless, in the perinuclear region of infected
269 cells, we observed the appearance of a complex membranous network that anti-correlates with
270 vgRNA and dsRNA, with visible encapsulation of vgRNA and dsRNA clusters (Supplementary Fig.
271 S7, S8). Taken together, these findings indicate that each vgRNA-dsRNA-RdRp cluster is located
272 inside a membrane-bound RO that originates from altered host ER transformed by SARS-CoV-2.

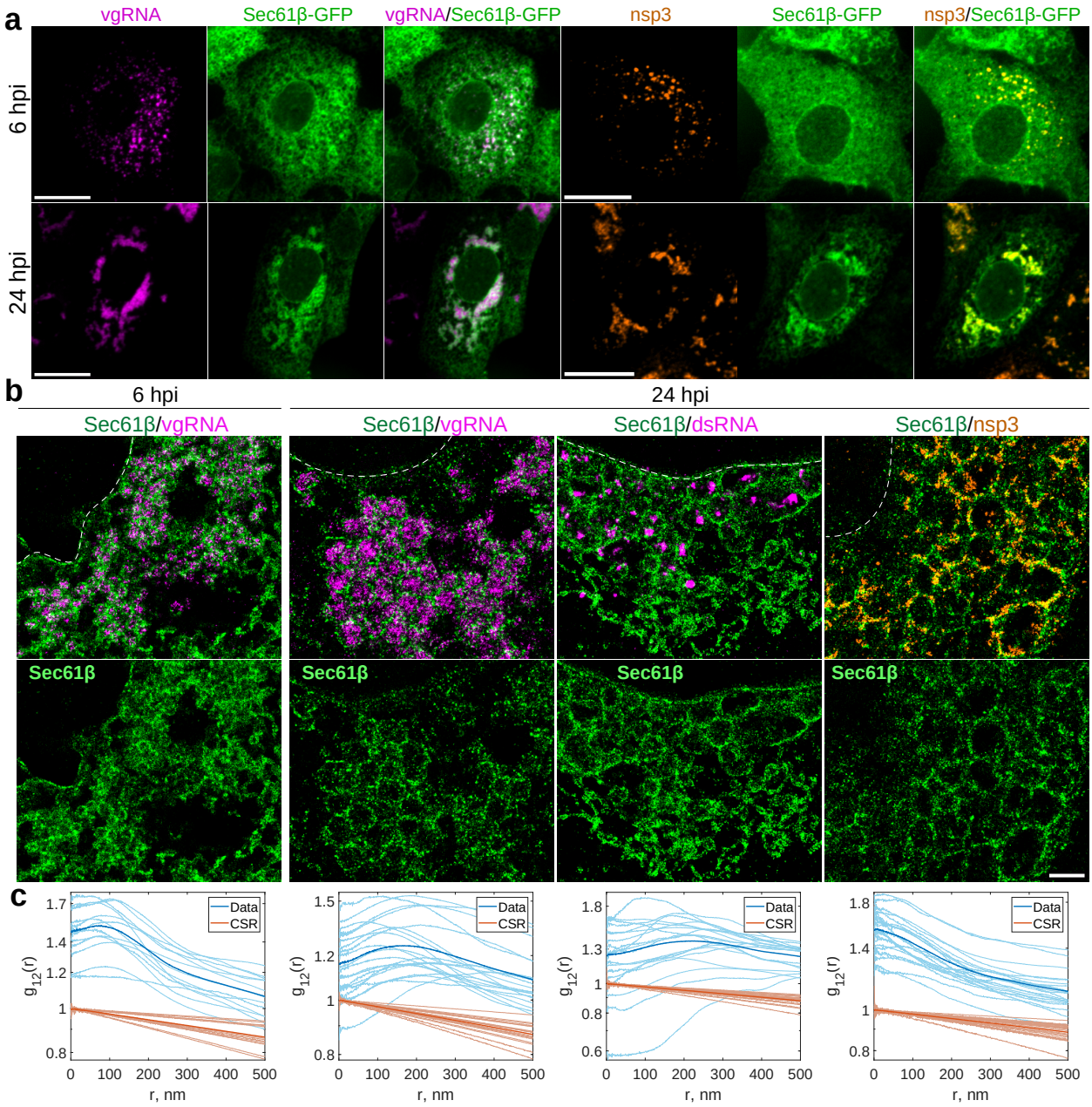

Fig. 4: vgRNA clusters are encapsulated in membranes of remodeled ER

a, Representative confocal images of SARS-CoV-2 infected cells indicate an appearance of dense perinuclear foci of Sec61β ER labelling (green) at 24 hpi that colocalizes with vgRNA and nsp3. **b**, SR images reveal concentric organization of Sec61β around vgRNA and dsRNA and colocalization of Sec61β with nsp3. **c**, Bivariate pair-correlation functions indicate anti-correlation of Sec61β with vgRNA and dsRNA and association of Sec61β with nsp3. Scale bars, 20 µm (**a**) and 1 µm (**b**). Dashed lines in **b** indicate the position of the cell nucleus.

282 *Nsp3 localizes at the surface of SARS-CoV-2 replication organelles*

283 Because the nsp3 protein of betacoronaviruses is essential for the DMV formation[31,32], and nsp3
284 is a constituent of a DMV molecular pore[16], we proceeded to localize this non-structural protein
285 to relate the ROs to the SARS-CoV-2-induced DMVs. At DL resolution, nsp3 labelling adopts a
286 pattern that colocalizes with vgRNA at both 6 and 24 hpi, similarly to dsRNA and nsp12 (Fig. 5a,
287 f). SR imaging of these cells, however, revealed striking nanoscale positioning of nsp3. At 6 hpi,
288 sparse nsp3 can be found surrounding isolated vgRNA clusters (Fig. 5c-d), while larger nsp3
289 aggregates are situated amidst bunched vgRNA clusters (Fig. 5e). At 24 hpi, nsp3 localizes at the
290 borders of the large vgRNA clusters, encircling them in incomplete rings and forming a partial
291 perinuclear network (Fig. 5g, i, j). Similar nsp3 arrangements can be observed in relation to dsRNA
292 (Supplementary Fig. S9).

293 The anti-correlation of vgRNA with nsp3 and dsRNA with nsp3 (Fig. 5, Supplementary Fig. S9)
294 closely resemble the pattern observed with vgRNA and dsRNA with Sec61β (Fig. 4, Supplementary
295 Fig. S6), suggesting that nsp3 may also be localized at the ER-derived membranous surface of the
296 ROs. To further confirm this hypothesis, we co-imaged nsp3 with Sec61β and CellMask (Fig. 4,
297 Supplementary Fig. S8, S10). The SR images and the pair-correlation analysis indicated
298 colocalization between nsp3 and both membrane markers at both time points (Fig. 4b-c,
299 Supplementary Fig. S8, S10), confirming that nsp3 localizes on the membranes encircling the
300 SARS-CoV-2 ROs.

301 Besides these characteristic localization patterns of nsp3, we observed a few cells with two
302 different phenotypes at 24 hpi, one with an ER-like network that occupies large regions in the
303 cytoplasm (Supplementary Fig. S11a), and another one with nsp3 densely diffused throughout
304 the whole cytoplasm (Supplementary Fig. S11b). The ER-like network may represent nsp3
305 proteins being heavily translated on ER membrane, while nsp3 proteins found outside the
306 perinuclear region are less likely to be associated with the SARS-CoV-2 replication process and
307 might represent other nsp3 functions, such as a papain-like proteolytic function[33] or post-
308 translational modification of host proteins[34], which can become objects of future SR studies.

309 The localization of nsp3 at the surface of isolated vgRNA-dsRNA clusters at 6 hpi is consistent with
310 the localization of molecular pores on the DMV membrane observed by cryo-EM[16]. At late
311 infection times, DMVs have been observed to merge into vesicle packets (VPs)[5] that are also likely
312 to contain pores, however molecular pores in the VP membranes have not yet been studied in
313 detail to our knowledge. Nevertheless, previous studies report that in late infection the
314 perinuclear region becomes filled with DMVs and VPs[26] that strongly resemble the ROs reported
315 here. The size of vgRNA clusters at 6 hpi and at 24 hpi from our data is similar to the previously
316 reported size of DMVs and VPs, correspondingly[5]. Taken together, our results provide evidence
317 that vgRNA accumulates, in DMVs at 6 hpi and in VPs at 24 hpi. dsRNA clusters occur within the
318 same vesicles but occupy distinct parts of them. Our data suggests a model where SARS-CoV-2
319 RNA is replicated and transcribed within these DMVs and VPs as highlighted by the proximal
320 localizations of RdRp.

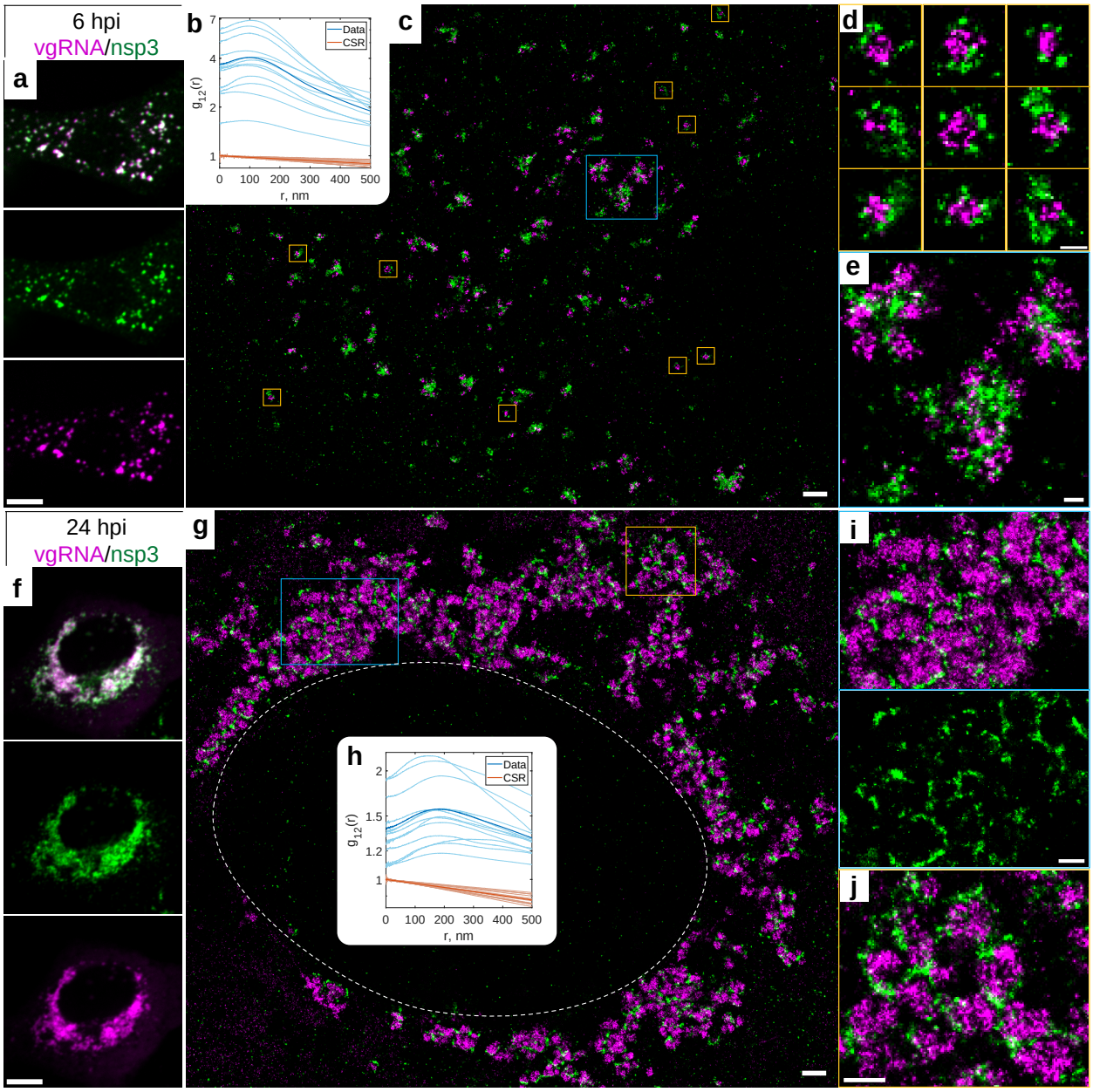

Fig. 5: Nsp3 localizes at the surface of vgRNA clusters

a, Representative confocal images of a SARS-CoV-2 infected cell display DL colocalization between punctate vgRNA (magenta) and nsp3 (green) labeling at 6 hpi. **b**, Bivariate pair-correlation functions calculated between the SR localizations of vgRNA and nsp3 indicate nanoscale anti-correlation of these targets at 6 hpi. **c**, Representative SR image of the cytoplasm of a SARS-CoV-2 infected cell at 6 hpi. **d**, Zoomed-in images of selected vgRNA particles (yellow boxes in **c**) indicate the localization of nsp3 at the surface of the vgRNA clusters. **e**, Magnified region with aggregates of vgRNA clusters (blue box in **c**) displays dense nsp3 localization in the core of these aggregates. **f**, Confocal images indicate that vgRNA and nsp3 occupy approximately the same regions in a SARS-CoV-2 infected cell at 24 hpi. **g**, Representative SR image of a SARS-CoV-2

332 infected cell at 24 hpi. **h**, Bivariate pair-correlation functions indicate nanoscale anti-correlation
333 between vgRNA and nsp3 at 24hpi. **i**-**j**, Magnified regions of the SR image (colored boxes in **g**)
334 show that nsp3 localizes in interstitial regions or encapsulates vgRNA clusters. Scale bars, 10 µm
335 (**a**, **f**), 1 µm (**c**, **g**), 500 nm (**i**, **j**), 200nm (**d**, **e**). Dashed line in **g** indicates the position of the cell
336 nucleus.

337

338

339 **Discussion**

340 Previous biochemical and EM studies allowed researchers to build models of the intracellular life
341 cycle of SARS-CoV-2[35-37]; however, precise localization of specific viral proteins and RNA molecules
342 is challenging due to lack of specific contrast in EM and low resolution in DL fluorescence
343 microscopy. SR fluorescence microscopy is well suited for coronavirus studies in cells as it provides
344 both specific contrast and high resolution (~20 nm and below depending upon photons
345 collected[38]). However, to date few studies have employed this method for coronavirus biology[15],
346 even less for SARS-CoV-2[27,39,40], and none of them focused on the SARS-CoV-2 replication process
347 in detail. Here we apply SR fluorescence microscopy to precisely localize the key players of SARS-
348 CoV-2 replication at different time points in infected cells. Building upon a previously developed
349 method for simultaneous labelling of coronavirus vgRNA with dsRNA and protein
350 immunofluorescence[15], and using improved fixation and multi-color SR imaging protocols (see
351 Methods), we obtain and quantify the appearance and molecular compositions of ROs of SARS-
352 CoV-2 in cells at different stages of infection.

353 In this study, our results taken together depict a compelling and novel picture of ROs containing
354 various molecules including vgRNA, dsRNA, RdRp, nsp3, and ER membrane (Fig. 6). In this model,
355 we compare the organization of ROs at early and late stages of infection and show how specific
356 RNA and protein molecules are spatially organized in ROs. Compared to the simpler and less
357 pathogenic HCoV-229E case, SARS-CoV-2 appears to generate more complex clusters of vgRNA,
358 and with the imaging of viral proteins involved in vgRNA replication and in DMV formation, the
359 structural importance of ROs is now clear.

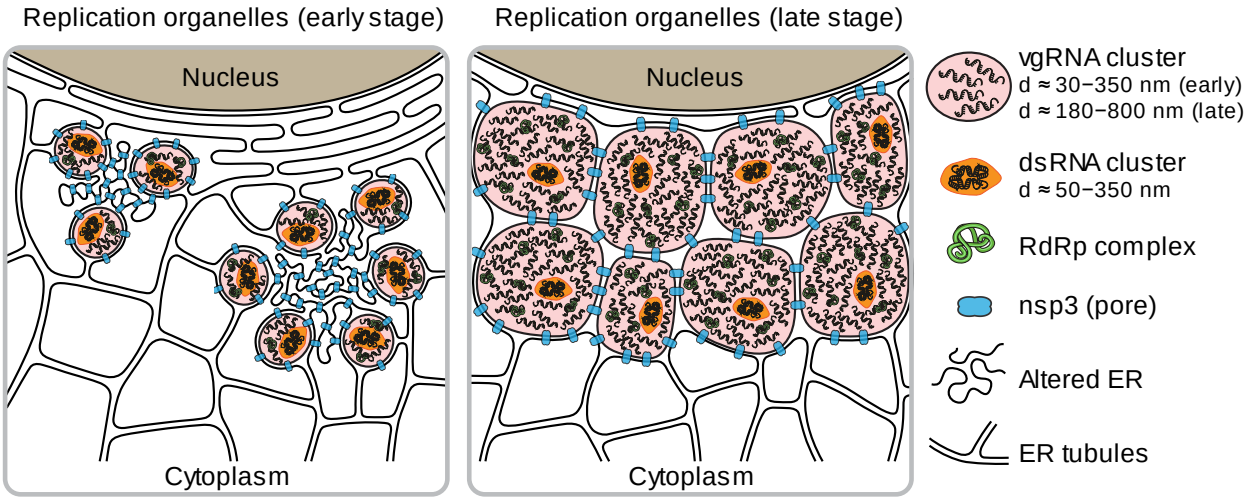

Fig. 6: Proposed model for SARS-CoV-2 replication organelles containing various RNA and protein molecules at early and late stages of infection.

The detailed intracellular localization of the central SARS-CoV-2 component, vgRNA, has remained vague in the literature. Our RNA FISH method[15] targets specific sequences in vgRNA (Fig. 1a) and detects single vgRNA molecules (Supplementary Fig. S1, S3a), allowing counting of the number of vgRNA molecules within specific regions (Supplementary Fig. S3b-c). We find for the first time that most cellular vgRNA localizes into dense clusters of an approximately round shape that grow and migrate to the perinuclear region as infection time increases. We show that these clusters appear confined in membranous vesicles derived from ER as emphasized by the localization of Sec61β and CellMask at their surface (Fig. 4b, Supplementary Fig. S4, S5, S8). From comparison with earlier EM images[5,16,26] and from nsp3 localization at their surface[16] (Fig. 5), we can conclude that these vesicles are most likely DMVs at an early-mid infection time that grow and merge into VPs as infection progresses.

Previously, metabolic radioactive labelling was used to localize newly synthesized RNA in SARS-CoV-1 and MERS-CoV-infected cells to DMVs[4]. However, metabolic labelling could only localize a fraction of vgRNA molecules with little sequence specificity and with a background of newly transcribed cellular RNA and viral sgRNA. Here, we specifically label vgRNA of SARS-CoV-2 for SR microscopy and show that it also localizes in patterns that suggest confinement in DMVs, confirming the earlier findings on SARS-CoV-1 and MERS-CoV[4].

381 Previous studies also suggested the presence of dsRNA in DMVs of SARS-CoV-1[3] and SARS-CoV-
382 2[5]. EM images of DMVs often display a complex filamentous network in their interior, that was
383 attributed to viral RNA molecules[5]. However, the exact type of these RNAs was not determined
384 due to the absence of specific labelling. As one might expect, single-stranded vgRNA can form a
385 secondary structure that includes many short dsRNA fragments *e.g.*, in stem loops[41,42]. This makes
386 it difficult to distinguish between viral dsRNA and vgRNA by measuring the diameter of the
387 filaments, taking into account that the detection probability of ssRNA might be lower due to a
388 decreased EM contrast for ssRNA than for dsRNA. Reported abundant branching of filaments in
389 DMVs[5], however, is typical for ssRNA secondary structures[43]. Indeed, there was some evidence in
390 the literature about presence of both dsRNA and vgRNA in DMVs; however, to our knowledge,
391 there was no simultaneous observation of both vgRNA and dsRNA within the same DMVs.

392 Here we use the J2 anti-dsRNA antibody that recognizes only long dsRNA fragments (≥ 40bp) with
393 no detection of the ssRNA secondary structures[44,45]. Two-color SR imaging revealed for the first
394 time that most dsRNA and vgRNA are located within the same DMVs and VPs, occupying distinct
395 regions of these vesicles, and adopting an anti-correlation pattern at short distances ($r < 100$ nm)
396 at 24 hpi (Fig. 2). Another novel observation is the relatively constant amount of dsRNA and a
397 slight decrease in dsRNA cluster size between 6 and 24 hpi despite the huge change in the vgRNA
398 landscape (Fig. 2).

399 It has been proposed that the RdRp complex of SARS-CoV-1 is located at convoluted membranes
400 and inside DMVs based on immunogold labelling of nsp8[3]. However, nsp8 has intracellular
401 functions other than as an RdRp accessory subunit[46,47] that might be exercised at the convoluted
402 membranes. Here we label the catalytic RdRp subunit, nsp12[22], and find that it mostly localizes
403 to the vgRNA clusters at both 6 and 24 hpi (Fig. 3), suggesting that SARS-CoV-2 replication and
404 transcription occurs preferentially in the vgRNA-filled ROs, where dsRNA resides as well.

405 Nsp3 of betacoronaviruses (SARS-CoV-1, MERS-CoV and MHV) was previously localized to the
406 convoluted membranes and to the DMV membranes using immuno-EM[3,4,48,49] and cryo-ET[16];
407 however, these studies were limited to early-mid infection at 8-12 hpi. In our study, we report
408 two localization patterns of nsp3 of SARS-CoV-2 at 6hpi: 1) sparse nsp3 at the surface of isolated

409 vgRNA-dsRNA clusters (Fig. 5d, Supplementary Fig. S9a); 2) dense nsp3 within the accumulations
410 of vgRNA-dsRNA clusters (Fig. 5e, Supplementary Fig. S9a). While the first pattern most likely
411 corresponds to the RO/DMV membranes considering the role of nsp3 as a DMV pore[16], the
412 second one resembles a pattern found in other coronaviruses that was attributed to the
413 convoluted membranes[3,4,50]. Convoluted membranes are typically found within dense groups of
414 DMVs in early-mid infection[3,4] and localization of nsp3 on them might represent early steps of
415 viral transformation of ER into DMVs. We found this nsp3 pattern anti-correlated with vgRNA (Fig.
416 5c, e) and with dsRNA (Supplementary Fig. S9a-b), suggesting little to no vgRNA or dsRNA at the
417 convoluted membranes, in line with previous studies on other coronaviruses[4].

418 At 24 hpi, we did not observe these early infection patterns of nsp3 localization. Instead, we show
419 for the first time that at 24 hpi, nsp3 densely localizes at the membranes that separate large
420 vgRNA clusters and grows into a considerable perinuclear network that contains the ROs (Fig. 5g,
421 i-j, Supplementary Fig. S9c). Since the molecular pores of VPs have not yet been investigated in
422 detail, we can speculate that this late infection nsp3 pattern corresponds to the pores of VPs that
423 should also be much denser than those of isolated DMVs, considering the increased density of
424 nsp3 labelling. Additional rare phenotypes of nsp3 localization that we also report for the first
425 time (Supplementary Fig. S11) illustrate the variability of SARS-CoV-2 infection course and should
426 lead to further research on the other intracellular functions of this viral protein.

427 Taken together, we investigated several key factors of SARS-CoV-2 replication: vgRNA, dsRNA,
428 RdRp and nsp3 inside infected cells with SR microscopy for the first time. We discovered and
429 characterized perinuclear clusters of vgRNA and demonstrated by RdRp labelling that they
430 associate with SARS-CoV-2 ROs. We found that the ROs also contain dsRNA and are encapsulated
431 in ER-derived membranes. Using SR data on nsp3, we conclude that these virus-induced
432 organelles correspond to DMVs.

433 This study expands the knowledge of the biology of coronaviruses and opens new possibilities for
434 therapeutics against SARS-CoV-2. Careful examination of the organization of ROs may provide
435 new avenues to target the organelles to disrupt SARS-CoV-2 replication and transcription.
436 Examining localization patterns for different viral variants or in different host cells will be useful

437 to broaden understanding of the viral infection. It will also be important to examine how the
438 structures reported in this study change upon the addition of drug treatments. Our imaging
439 approach may also offer insights into long COVID by investigating cells that are infected by SARS-
440 CoV-2 that may still contain RO-like structures after symptoms disappear.

441

442

443 **Methods**

444 *Antibodies*

445 Primary antibodies and the optimal dilutions and concentrations used are as follows: goat
446 polyclonal anti-spike S2 (Novus Biologicals, AF10774-SP, 1:20, 10 µg/mL), mouse monoclonal anti-
447 dsRNA (SCICONS, 10010200, 1:200, 5 µg/mL), rabbit polyclonal anti-RdRp/nsp12 (Sigma-Aldrich,
448 SAB3501287-100UG, 1:500, 2 µg/mL), mouse monoclonal anti-nucleocapsid (Thermo Fisher,
449 MA5-29981, 1:500, 2 µg/mL), rabbit polyclonal anti-nsp3 (Thermo Fisher, PA5-116947, 1:134, 5
450 µg/mL), sheep polyclonal anti-GFP (Bio-Rad, 4745-1051, 1:1000, 5 µg/mL), and rabbit polyclonal
451 anti-GFP (Novus Biologicals, NB600-308SS, 1:163, 5 µg/mL). Secondary antibodies and the
452 optimal dilutions and concentrations used are as follows: AF647-conjugated donkey anti-mouse
453 IgG (Thermo Fisher, A-31571, 1:500, 4 µg/mL), AF647-conjugated donkey anti-rabbit IgG (Thermo
454 Fisher, A-31573, 1:500, 4 µg/mL), AF647-conjugated donkey anti-sheep IgG (Thermo Fisher, A-
455 21448, 1:500, 4 µg/mL), CF568-conjugated donkey anti-goat IgG (Sigma-Aldrich, SAB4600074-
456 50UL, 1:500, 4 µg/mL), CF568-conjugated donkey anti-rabbit IgG (Sigma-Aldrich, SAB4600076-
457 50UL, 1:500, 4 µg/mL), CF568-conjugated donkey anti-mouse IgG (Sigma-Aldrich, SAB4600075-
458 50UL, 1:500, 4 µg/mL), and CF568-conjugated donkey anti-sheep IgG (Sigma-Aldrich,
459 SAB4600078-50UL, 1:500, 4 µg/mL).

460

461 *Culture of cell lines*

462 The Vero E6 cells (African green monkey kidney epithelial cells, ATCC, CRL-1586), HEK293T cells
463 (human embryonic kidney epithelial cells, ATCC, CRL-3216), and Vero E6-TMPRSS2 cells were
464 cultured in Dulbecco's modified Eagle medium (DMEM) with GlutaMAX, 25 mM D-Glucose, and
465 1 mM sodium pyruvate (Gibco, 10569010) in 10% FBS (Sigma-Aldrich, F0926) at 37°C and 5% CO2
466 in a humidified incubator. Cell lines were not authenticated after purchase prior to use. For Vero
467 E6-TMPRSS2, Geneticin (G418) was added at a final concentration of 1mg/ml.

468

469 *Lentivirus production for ER labeling with Sec61β*

470 To produce lentivirus, HEK293T cells were cultured in 10-cm dishes and transiently transfected
471 with 9 µg lentiviral plasmid pLV-ER-GFP (Addgene, 80069, a gift from Pantelis Tsoulfas), 8 µg
472 pCMV-dR8.91, and 1 µg PMD2.G packaging plasmids using 25 µL TransIT-LT1 Transfection Reagent
473 (Mirus, MIR 2306). After 72 h of transfection, supernatant was filtered through 0.45 µm filters,
474 concentrated using Lentivirus Precipitation Solution (ALSTEM, VC100) at 4°C overnight, and
475 centrifuged at 1,500x g for 30 min at 4°C to collect virus pellets. The virus pellets were
476 resuspended in cold DMEM for storage at -80°C for transduction of cells.

477

478 *Generation of stable cell line*

479 To generate a Vero E6 cell line stably expressing Sec61β-GFP, $2x10^5$ Vero E6 cells were seeded in
480 one well of a 6-well plate and infected with one quarter of concentrated lentivirus expressing pLV-
481 ER-GFP produced from one 10-cm dish of HEK293T cells while seeding. After two days incubation,
482 monoclonal cells expressing GFP were sorted out using a SONY SH800S sorter. These transduced
483 cells were only used for ER imaging; all other experiments used wild type (WT) cells.

484

485 *SARS-CoV-2 viral stocks preparation*

486 The SARS-CoV-2 WA 1, isolate USA-WA1/2020 (NR-52281, BEI Resources) was passaged 3 times
487 in Vero E6-TMPRSS2 cells as previously described[51,52]. Briefly, a Vero E6-TMPRSS2 monolayer was
488 infected with virus obtained from BEI; post 72 hours of infection (hpi), P1 virus-containing tissue
489 culture supernatants were collected and stored at -80°C. Following titration, P1 virus stock was
490 used to generate a P2 stock by infecting Vero E6 TMPRSS2 monolayers with multiplicity of
491 infection (MOI) of 0.0001 for 72 hours. P2 virus was passaged again in Vero E6-TMPRSS2 cells to
492 obtain P3 stock. Viral titers were determined by standard plaque assay on Vero E6 cells.

493

494 *Infection of cells by SARS-CoV-2*

495 Vero E6 cells previously cultured in 8-well μ-slides were infected in the BSL3 facility with SARS-
496 CoV-2 WA 1 (USA212 WA1/2020) in triplicates (MOI=0.5 SARS-CoV-2 WA1 (P3)) at an MOI of 2 for
497 6 hpi and MOI of 0.2 for 24 hpi. After 6 and 24 hrs of incubation, cells were washed with PBS and
498 fixed by 4% PFA (Electron Microscopy Sciences #15710) and 0.1% glutaraldehyde (Electron
499 Microscopy Sciences #16350) in PBS for 1 hour and removed from BSL3 for further processing. All
500 work involving viral stock preparation and infection using WT SARS-CoV-2 was conducted at the
501 high containment BSL3 facility of Stanford University according to CDC and institutional
502 guidelines. All the experiments were performed using a P3 SARS-CoV-2 USA-WA1/2020,
503 containing 100% WT population with no deletion in the spike multi-basic cleavage site.

504

505 *Synthesis of the RNA FISH probes*

506 vgRNA FISH probes targeting the ORF1a region of SARS-CoV-2[17] were ordered with 5AmMC6
507 modifications from Integrated DNA Technologies, Inc. in plate format of 25 nmol scale with
508 standard desalting. Each probe was dissolved in water to a final concentration of 100 μM. The
509 same set of probes was combined with equal volumes of each probe to get a stock of 100 μM
510 mixed probes. The mixed probes were further desalted using ethanol precipitation. Briefly, 120
511 μL 100 μM probes were mixed with 12 μL 3 M sodium acetate (pH 5.5), followed by 400 μL
512 ethanol. After precipitation at -80C overnight, probes were pelleted through centrifugation at
513 12,000x g for 10 min at 4°C, washed with precooled 70% (vol./vol.) ethanol three times, air dried,
514 and dissolved in water to make a 100 μM solution of probes. Then, 18 μL 100 μM probes were
515 mixed with 2 μL 1 M $NaHCO_3$ (pH 8.5), followed by 100 μg Alexa Fluor™ 647 succinimidyl ester
516 (NHS) (Invitrogen, A37573) or CF568 succinimidyl ester (NHS) (Biotium, 92131) dissolved in 2 μL
517 dry DMSO (Invitrogen, D12345). The mixture was incubated for 3 days at 37C in the dark for
518 conjugation and purified for 3 rounds using Monarch PCR & DNA Cleanup Kit (5 μg) (NEB, T1030S)
519 following the manufacturer's instructions. The estimated labeling efficiency of probes was
520 calculated using the following equation:

521 $$Modification\ ratio = \frac{20}{(A_{base} \times \varepsilon_{dye})\ /\ (A_{dye} \times \varepsilon_{base})}$$

522 where ε_{dye} is 239,000 $cm^{-1}M^{-1}$, ε_{base} is 8,919 $cm^{-1}M^{-1}$, A_{base} is the absorbance of the nucleic acid at
523 260 nm, and A_{dye} is the absorbance of the dye at 650 nm. For the probes labeled with CF568, ε_{dye}
524 is 100,000 $cm^{-1}M^{-1}$, ε_{base} is 8,919 $cm^{-1}M^{-1}$, A_{base} is the absorbance of the nucleic acid at 260 nm,
525 and A_{dye} is the absorbance of the dye at 562 nm.

526

527 *RNA FISH, immunofluorescence (IF), and CellMask staining*

528 Fixed cells from BLS3 as described above were washed twice with a freshly prepared 0.1% $NaBH_4$
529 solution at room temperature for 5 min, and washed with PBS three times. For staining without
530 CellMask (Thermo Fisher, C10046), cells were permeabilized in 70% ethanol at 4°C overnight. For
531 CellMask staining, cells were permeabilized in 0.1% Triton X-100 at room temperature for 30 min.

532 For RNA FISH staining, permeabilized cells were washed with 200 µL Wash Buffer A [40 µL Stellaris
533 RNA FISH Wash Buffer A (LGC Biosearch Technologies, SMF-WA1-60), 20 µL deionized formamide,
534 140 µL H2O] at room temperature for 5 min, and incubated with 110 µL Hybridization Buffer [99
535 µL Stellaris RNA FISH Hybridization Buffer (LGC Biosearch Technologies, SMF-HB1-10), 11 µL
536 deionized formamide] containing 1.1 µL 12.5 µM vgRNA FISH probes for 4 hours at 37°C in the
537 dark. Then cells were washed with Wash Buffer A for 30 min at 37°C in the dark, washed with
538 Wash Buffer A containing DAPI for 30 min at 37°C in the dark, and stored in Wash Buffer B (LGC
539 Biosearch Technologies, SMF-WB1-20) for imaging. DAPI was only added to the samples for
540 confocal imaging and not added to the samples for SR imaging.

541 For IF staining with antibodies, permeabilized cells were washed with PBS twice, incubated with
542 3% BSA in PBS at room temperature for 30 min, and incubated with primary antibodies in PBS at
543 37°C for 1 hour. After incubation with primary antibodies, cells were washed twice with PBST
544 buffer (0.1% Tween-20 in PBS) at room temperature for 5 min, washed with PBS once, incubated
545 with secondary antibodies in PBS at room temperature for 30 min, washed with PBST buffer three
546 times at room temperature for 5 min, and stored in PBS for imaging.

547 For simultaneous RNA FISH and IF staining, permeabilized cells were washed with 200 µL Wash
548 Buffer A at room temperature for 5 min, and incubated with 110 µL Hybridization Buffer (99 µL

549 Stellaris RNA FISH Hybridization Buffer, 11 µL deionized formamide) containing 1.1 µL 12.5 µM
550 vgRNA FISH probes, 1 U/µL RNase inhibitor (NxGen, F83923-1), and primary antibodies for 4 hours
551 at 37°C in the dark. Then cells were washed with 2xSSC buffer once, washed with Wash Buffer A
552 containing secondary antibodies for 30 min at 37°C in the dark, washed with Wash Buffer A for
553 30 min at 37°C in the dark, washed with Wash Buffer B once, and stored in Wash Buffer B for
554 imaging. For CellMask staining, several more steps were performed from here. Cells were washed
555 with PBS once, stained with 1:20k CellMask and 1 U/µL RNase inhibitor in PBS for 20 min at room
556 temperature in the dark, and washed with PBS three times before imaging.

557

558 *RNA FISH and IF staining of purified virions*

559 8-well µ-slides (ibidi, 80827-90) were first treated with poly-D-lysine solution (Thermo Fisher,
560 A3890401) at 4°C overnight. Then in the BSL3 facility, the poly-D-lysine solution was removed and
561 150 µL SARS-CoV-2 WA1 (P3) virus solution of titer 1.82×10^5 PFU/mL was added into one well of
562 poly-D-lysine-treated 8-well µ-slides for incubation at 4°C for 24 hours to coat the virions onto
563 the surface of the well. After incubation, the medium containing virions was removed and the
564 well was washed with PBS twice. Virions on the surface of the well were fixed with 4% PFA in PBS
565 for 1 hour at room temperature and the sample was removed from BSL3. The sample was washed
566 twice with a freshly prepared 0.1% $NaBH_4$ solution at room temperature for 5 min, and then
567 washed with PBS three times. The fixed virions were permeabilized in 70% ethanol at 4°C
568 overnight and washed with PBS twice. For the group with Proteinase K digestion, virions were
569 incubated with 0.2 mg/mL Proteinase K (NEB #P8107S) in 120 µL PBS at 37°C for 30 min and
570 washed with PBST buffer three times. Virions were washed with Wash Buffer A once and
571 incubated with 110 µL Hybridization Buffer (99 µL Stellaris RNA FISH Hybridization Buffer, 11 µL
572 deionized formamide) containing 1.1 µL 12.5 µM vgRNA FISH probes, 1 U/µL RNase inhibitor, and
573 primary antibodies for 4 hours at 37°C in the dark. Then virions were washed with 2xSSC buffer
574 once, washed with Wash Buffer A containing secondary antibodies for 30 min at 37°C in the dark,
575 washed with Wash Buffer A for 30 min at 37°C in the dark, washed with Wash Buffer B once, and
576 stored in Wash Buffer B for imaging.

577

578 *Spinning disk confocal microscopy*

579 Confocal microscopy was performed at the Stanford University Cell Sciences Imaging Core Facility
580 with a Nikon TiE inverted spinning disk confocal microscope (SDCM) equipped with a
581 Photometrics Prime 95B camera, a CSU-X1 confocal scanner unit with microlenses, and 405 nm,
582 488 nm, 561 nm, and 642 nm lasers, using the 60x/1.27 NA PLAN APO IR water immersion
583 objective. Images were taken using NIS Elements software version 4.60 with Z stacks at 0.3 µm
584 steps. The camera pixel size of SDCM is 0.183 µm/pixel and the pinhole size is 50 µm. Only one Z
585 slice is used for all images shown.

586

587 *Analysis of confocal data*

588 To extract the intensity of vgRNA, dsRNA and RdRp in each infected cell (Supplementary Fig. S2),
589 the summation projection of each z stack was created by Fiji[53]. The intensity of each target species
590 in each cell was measured by Fiji, subtracting the background of the same color channel. The
591 infected cells were characterized manually into three types based on the morphology of vgRNA.
592 Type 1 shows scattered dot-like localization of vgRNA. Type 3 shows large clustered vgRNA. Type
593 2 contains features of both type 1 and type 3.

594

595 *Optimization of antibody concentrations*

596 We optimized the concentration of antibodies in this study by quantifying their signal-to-
597 background ratio (SBR), where the signal is the brightness of the IF labelling in the cells that
598 express the given target (virus-infected sample or cells expressing Sec61β-GFP), and the
599 background is the brightness in the negative control cells (not-infected or WT cells).

600 To optimize the concentration of primary antibodies against the viral targets, different
601 concentrations of the primary antibody were applied to stain Vero E6 cells in SARS-CoV-2-infected
602 and not-infected samples under a constant secondary antibody concentration (Supplementary

Fig. S12). To optimize the concentration of secondary antibodies, different concentrations of the secondary antibody were applied to stain Vero E6 cells in infected (virus+) and not-infected (virus−) samples under a constant primary antibody concentration (Supplementary Fig. S13). For each cell, a 11 pixel x 11 pixel box was drawn in the region with brightest signal in the cell and the mean intensity within that region was measured to represent the intensity of target antibody in that cell. The SBR was calculated, after subtraction of the dark signal I_{dark}, using the following equation:

$$SBR = \frac{< I_{virus+} - I_{dark} >}{< I_{virus-} - I_{dark} >}$$

To optimize the concentration of the anti-GFP antibodies, different concentrations of primary antibody were applied to stain Vero E6 Sec61B-GFP cells and WT Vero E6 cells under a constant secondary antibody concentration (Supplementary Fig. S12). For each cell, a 11 pixel x 11 pixel box was drawn in the region with the brightest signal in the cell and the mean intensities of both the GFP and the antibody signals within that region were measured after subtraction of the dark signals. To account for the variable expression levels among different cells, the IF signal I_{IF} was normalized by the GFP signal I_{GFP} within the given region. The SBR was calculated using the following equation:

$$SBR = \frac{< I_{IF,Sec61B\text{-}GFP} / I_{GFP,Sec61B\text{-}GFP} >}{< I_{IF,WT} / I_{GFP,WT} >}$$

For the primary antibodies against GFP, nsp3, nucleocapsid, nsp12 and for the secondary antibody for the dsRNA labelling, we chose the antibody concentration that produces the highest SBR as the optimal concentration. For the primary antibodies against spike S2 and dsRNA and for the secondary antibody for the spike S2 labelling, we chose the concentration that yields the second highest SBR because it provides a significantly lower non-specific background with only a minor decrease of the estimated SBR.

628 *Optical setup for SR microscopy*

629 (d)STORM SR microscopy was performed on a custom-built system (Supplementary Fig. S14),
630 consisting of a Nikon Diaphot 200 inverted microscope frame with an oil-immersion objective
631 60x/1.35 NA (Olympus UPLSAPO60XO) and a Si EMCCD camera (Andor iXon Ultra 897). We used
632 642 nm and 560 nm 1W continuous-wave (CW) lasers (MPB Communications Inc.) for excitation
633 of AF647 or CellMask and CF568, accordingly. For reactivation of fluorophores from the dark state
634 we used a 405 nm 50 mW CW diode laser (Coherent OBIS). All laser beams were expanded and
635 co-aligned in free space and coupled into a square-core multi-mode fiber with a shaker for speckle
636 reduction (Newport F-DS-ASQR200-FC/PC). The output tip of the fiber (200 x 200 μm^2 core size)
637 was imaged with a 10x/0.25 NA objective and magnified to achieve a square illumination region
638 of 47.6 x 47.6 μm^2 with a constant intensity in the sample image plane of the main objective. The
639 fluorescence was split from the excitation light with a multi-band dichroic mirror
640 (ZT405/488/561/640rpcv2, Chroma) and filtered with dichroic filters (ZET635NF, ZET561NF,
641 T690LPxxr, all Chroma). The fluorescence of AF647 and CellMask was additionally filtered with a
642 band-pass filter (ET685/70M, Chroma) and that of CF568 with a combination of 561LP and
643 607/70BP (Semrock, EdgeBasic and BrightLine). The sample image was focused with a tube lens
644 (f = 400 mm) on the EMCCD camera, providing a pixel size of 117 x 117 nm^2 in sample coordinates.

645 Axial drift was compensated with a custom Focus Lock system[54]. We used an 808 nm fiber-coupled
646 diode laser (Thorlabs S1FC808) whose output fiber tip was conjugated with the back focal plane
647 of the imaging objective, allowing changing the angle of this beam out of the objective by
648 translating the fiber tip (Supplementary Fig. S14). This inclined beam was partially reflected from
649 the coverslip-water interface and the reflected beam was focused with a cylindrical lens onto a
650 CMOS sensor (UI-3240CP-NIR, IDS Imaging). The 808 nm beam was aligned such that the image
651 of the reflected beam would shift laterally when the axial position of the sample changes. The
652 sample was mounted on two stacked piezo stages (U-780.DOS for coarse and P-545.3C8S for fine
653 movement, both Physik Instrumente). The position of the reflected beam image was recorded
654 when the sample was set at the desired Z position for imaging. During imaging, the Z-position of
655 the fine stage was directed to move proportionally to the shift of the reflected beam image from

656 the recorded position, compensating for Z-drift. The Focus Lock control code was programmed in
657 Matlab (MathWorks, Inc.).

658

659 *SR imaging procedure*

660 For (d)STORM, the sample chamber was filled with 300 µl of a photoblinking buffer consisting of
661 200 U/ml glucose oxidase, 1000 U/ml catalase, 10% w/v glucose, 200 mM Tris-HCl pH 8.0, 15 mM
662 NaCl and 50 mM cysteamine. The buffer was prepared using the following stock solutions[38]: 1)
663 4 kU/ml glucose oxidase (G2133, Sigma), 20 kU/ml catalase (C1345, Sigma), 25 mM KCl (P217,
664 Fisher), 4 mM TCEP (646547, Sigma), 50% v/v glycerol (BP229, Fisher) and 22 mM Tris-HCl pH 7.0
665 (BP1756, Fisher), stored at −20 °C; 2) 1 M cysteamine-HCl (30080, Sigma), stored at −20 °C; 3) 37%
666 w/v glucose (49139, Sigma) with 56 mM NaCl (S271, Fisher) and 0.74 M Tris-HCl pH 8.0
667 (J22638.AE, Fisher), stored at +4 °C. For samples with RNA FISH labelling, the buffer was
668 supplemented with 1 U/µl of an RNase inhibitor (302811, LGC Biosearch Technologies).

669 The SR imaging started with a DL image of cells from each fluorophore at a low power (*e.g.*, 2
670 W/cm^2). For (d)STORM acquisitions, we began with AF647 or CellMask, followed by CF568. We
671 used an excitation power density of ~20 kW/cm^2 for shelving and blinking of CF568 and ~6-20
672 kW/cm^2 for AF647. The power density of the 405 nm illumination for both dyes was increased
673 from 0 to 50 W/cm^2 throughout an acquisition to keep the reactivation rate approximately
674 constant. The exposure time was 10.57 ms per frame and the calibrated EM gain was 43. The
675 image recording started after the initial shelving phase upon observation of clear SM blinking; the
676 blinking movies were acquired for approximately 60000 frames for each fluorophore.

677

678 *SR data analysis*

679 SM movies were processed with the ThunderStorm plugin[55] for Fiji. First, the images were filtered
680 with a wavelet filter with a b-spline order of 3 and a scale of 2. The coarse localizations were
681 found as local maxima with an 8-neighborhood connectivity and a threshold of 2·std(Wave.F1).
682 These localizations were weighted least squares-fitted with the integrated Gaussian model using

683 a radius of 4 pixels and an initial sigma of 1.1. Then, we performed drift correction estimated by
684 cross-correlation between successive subsets of localizations. For further processing, we kept
685 only localizations with fitted sigma between 160 nm and 80 nm.

686 For image registration, we imaged 200 nm TetraSpeck beads (T7280, Thermo Fisher Scientific) in
687 both channels, whose images were processed similarly to the SM movies. The transformation
688 between the channels was calculated using an affine transformation with help of Matlab function
689 'fitgeotrans'. The calculated transformation was then applied to the CF568 localizations using a
690 Matlab function 'transformPointsInverse'.

691 Localizations found within 50 nm on consecutive frames that could originate from multiple
692 localizations of a single molecule were treated in two ways. For SR images, these localizations
693 were refined to suppress overcounting by selecting them from a normal distribution with a mean
694 at the weighted mean of the initial localizations and a standard deviation (SD) that equals
695 $120 \cdot (N_{ph})^{-1/2}$ nm, where N_{ph} is the total number of photons acquired from all localizations in the
696 given consecutive series[38]. For data analysis other than SR image reconstruction, the localizations
697 of the consecutive series were reduced to a single localization at the weighted mean position.
698 The weights of localizations were proportional to the photon counts of these individual
699 localizations. SR images were reconstructed as 2D histograms with a bin size of 20 x 20 nm^2.
700 However, SR images where one of the channels contained the CellMask labelling had a bin size of
701 30 x 30 nm^2. SR images acquired with CellMask were additionally filtered with a Gaussian filter
702 with $\sigma = 0.5$ pixels.

703

704 *Cluster analysis with BIC-GMM*

705 Gaussian Mixture Models (GMM) implemented in Python were fitted to vgRNA and dsRNA
706 localization datasets, yielding a representation of localization densities as a collection of
707 potentially elliptical and/or rotated 2D Gaussians. The number of components most suitable for
708 each field of view was determined using an iterative grid search, evaluating 4 candidate GMMs
709 using the Bayesian Information Criterion (BIC)[56]. The first grid iteration tested [1, 2500]

710 components with test points t_i = { 1,834,1667,2500 } , where i denotes the index in the set such
711 that t_0 = 1. For each iteration of the grid search, the model with the lowest BIC (corresponding to
712 the best candidate), t_k was selected, and the next iteration of the grid was narrowed, to be
713 bounded by [$t_{max\ (k-1,\ 0)}$ + 1, $t_{min\ (k+1,\ 3)}$ − 1], until the stride of the grid was 1 component, or the test
714 point with the best BIC was on a rail (k = 0 or 3). To reduce memory requirements, this GMM
715 optimization was performed on a random subset of up to 200,000 localizations from each data
716 set, but the optimized GMM was then used to predict a component assignment for all original
717 localizations. These components were regarded as clusters, and refined by removing localizations
718 with a log probability of being an event from their assigned Gaussian component of less than −25.
719 The radius of gyration, *Rg*, was then calculated for each cluster, and the number of localizations
720 in each cluster, N_{loc}, was used to approximate a cluster density as $\delta = N_{loc} / (\pi \cdot Rg^2)$. Clusters with
721 δ below a threshold of 0.008 localizations/nm^2 for dsDNA, or below an ROI-dependent threshold
722 between 0.005 and 0.013 localizations/nm^2 for vgRNA, were removed from further quantification
723 as sparse background. This analysis and resulting visualizations were carried out in the PYthon
724 Microscopy Environment (https://doi.org/10.5281/zenodo.4289803)[57], using a plugin
725 (github.com/barentine/bic-gmm) and the scikit-learn GMM implementation[58].

726

727 *Counting of vgRNA molecules in the clusters*

728 The number of vgRNA molecules in a vgRNA cluster was defined as a quotient between the
729 number of vgRNA-FISH localizations in the cluster and the average number of localizations
730 produced by a single FISH-labelled vgRNA molecule in the given cell. The average number of
731 localizations per vgRNA molecule was estimated from isolated nanoscale vgRNA puncta in the
732 cytoplasm (Supplementary Fig. 3a). This number was defined as the median of the number of
733 localizations within 50 nm from each localization in the region with vgRNA puncta. The estimated
734 number of vgRNA molecules was calculated for every cluster determined by the BIC-GMM cluster
735 analysis and the median value per cell was shown in a chart (Supplementary Fig. 3b-c).

736

Counting of nsp12 puncta in the vgRNA clusters

The center of nsp12 puncta is obtained by fitting the SR images in ThunderStorm[55]. The SR localizations of nsp12 were first converted into a 2D histogram image with a bin size of 20 x 20 nm^2. The approximate localization of the center was found as a centroid of connected components with a threshold of 5·std(Wave.F1) without filter. These localizations were least squares-fitted with the integrated Gaussian model using a fitting radius of 2 pixels and an initial sigma of 0.4. We next removed duplicates among localizations within a 20 nm radius. The puncta whose sigma were smaller than 5 nm were further filtered out to avoid localizing single-pixel-sized background localizations. For each vgRNA cluster with its center and the radius of gyration (Rg) determined using BIC-GMM, we counted the number of nsp12 puncta within a 1.5·Rg distance of the center of the vgRNA cluster. For nsp12 puncta found within the cutoff distance of more than one vgRNA cluster, we assigned them to their closest cluster based on the relative distance d/Rg, with d being the distance between the center of the vgRNA cluster and center of the nsp12 punctum.

Bivariate pair-correlation functions

For calculation of bivariate pair-correlation functions[20] $g_{12}(r)$, we first manually selected the cytoplasmic regions with dense vgRNA clusters. The pair-correlation functions were calculated by counting the number of localizations of the second species within a distance between r and r+dr from each localization of the first species. These were normalized by dividing the number of localizations by the area of the corresponding ring of radii r and r+dr and by the average density of the second species in the region. Finally, the obtained numbers were averaged across the localizations of the first species. r was scanned over the range between 0 and 500 nm and dr was set to 1 nm. For the complete spatial randomness (CSR) case, a test CSR dataset was generated with the same average density as for the experimental case across the same ROI. $g_{12}(r)$ traces were calculated from these CSR datasets as described above. No edge effect correction was performed leading to a slight decrease of $g_{12}(r)$ at large r. Plots in the figures display experimental

764 and CSR $g_{12}(r)$ for each analyzed cell as faint lines as well as the mean $g_{12}(r)$ calculated from all
765 cells in bold lines.

766

767 *Estimation of RNA FISH labelling efficiency in virions*

768 Dye molecules inside virions were counted using fluorescence bleaching with SM calibration.
769 Virions attached to the coverslip were labelled using the RNA-FISH+IF protocol with PFA-only
770 fixation. The density of virions was around 0.5 μm^{-2} ensuring observation of most virions as single
771 DL spots without overlap (Supplementary Fig. S1a, d). vgRNA was FISH-labelled with AF647 and
772 spike protein was IF-stained with CF568. Glass-bottom chambers with virions were kept in PBS for
773 this experiment. Samples were illuminated with 642 nm light at 20 W/cm^2 and were imaged with
774 an exposure time of 200 ms and an EM gain of 43 until bleaching of all AF647 in the imaging
775 region (around 200 s). A separate DL image of spike was taken with 560 nm excitation. The AF647
776 bleaching movies were processed in ThunderStorm using a wavelet filter with a b-spline order of
777 3 and a scale of 2, a local maximum approximate localization with a threshold of 1.2·std(Wave.F1)
778 and an 8-neighborhood connectivity. These localizations were weighted least squares-fitted with
779 the integrated Gaussian model using a radius of 3 pixels and an initial sigma of 1.1. Then, we kept
780 only localizations with sigma < 160 nm & sigma > 80 nm and removed duplicates within 300 nm
781 on each frame.

782 Further processing was done in Matlab with a custom script. We considered only vgRNA-AF647
783 localizations that had a spike-CF568 signal within 200 nm to avoid counting AF647 molecules
784 outside virions. The bleaching time traces (Supplementary Fig. S1c, f) were found by searching in
785 consecutive frames within 200 nm of the localization from the first frame and allowing up to 5
786 empty frames between frames with detections. The number of bleaching steps was defined as
787 the rounded quotient between the initial and the final brightness of a spot in a time trace serving
788 as the SM calibration. For each bleaching trace, the initial brightness (in photons) was defined as
789 the median value of the brightness in the first 4 localizations and the final brightness as the
790 median brightness value of the last 4 localizations. If the trace contained only 7-8 detections, the
791 range for the initial and the final brightness was reduced to 3 frames; for traces with 5-6

792 detections, this was reduced to 2; for traces with 3-4 frames – to 1; for traces containing only 1
793 or 2 detections, the number of bleaching steps was set to 1. For each analyzed region containing
794 around 200 bleaching traces, the number of bleaching steps was fitted with a zero-truncated
795 Poisson distribution (Supplementary Fig. S1g-h). The expected values ± SD obtained from the fit
796 of 5 regions for each of not-treated and PK-treated cells are shown in a chart (Supplementary Fig.
797 S1i).

798

799

800 **Author contribution**

801 L.A., M.H., L.S.Q. and W.E.M. conceived the project. L.A. designed the optical set-up, performed
802 the SR acquisitions and data analysis. M.H. performed cell culture, labelling and confocal imaging.
803 Y.Z. performed confocal and SR data analysis and helped with sample preparation and confocal
804 imaging. J.G. performed SARS-CoV-2 infection experiments at the BSL-3 facility with staff listed in
805 the Acknowledgements. A.R.R. contributed to the concept and SR experiments at the early stages
806 of the project. A.E.S.B. designed the BIC-GMM cluster analysis method and contributed to the
807 optical set-up design. L.A and W.E.M. wrote the manuscript with input from all authors.

808

809 **Acknowledgements**

810 We thank Puja Patel and Amol Pohane for their assistance with the cell culturing in the BSL3
811 facility. We thank Leiping Zeng for sample preparation and discussion about the results and
812 experimental plan with the other authors. This work was supported in part by the National
813 Institute of General Medical Sciences Grant Nos. R35GM118067 (to W.E.M.) and the National
814 Institutes of Health Common Fund 4D Nucleome Program No. U01 DK127405 (to L.S.Q.). We also
815 acknowledge Stanford University Cell Sciences Imaging Core Facility (RRID:SCR_017787). L.S.Q. is
816 a Chan Zuckerberg Biohub Investigator, and W.E.M. is a Sarafan ChEM-H Fellow.

817

References

1. Schmidt, N. *et al.* The SARS-CoV-2 RNA–protein interactome in infected human cells. *Nature Microbiology* **6**, 339-353 (2021).
2. Flynn, R.A. *et al.* Discovery and functional interrogation of SARS-CoV-2 RNA-host protein interactions. *Cell* **184**, 2394-2411.e2316 (2021).
3. Knoops, K. *et al.* SARS-coronavirus replication is supported by a reticulovesicular network of modified endoplasmic reticulum. *PLoS Biol* **6**, e226 (2008).
4. Snijder, E.J. *et al.* A unifying structural and functional model of the coronavirus replication organelle: Tracking down RNA synthesis. *PLoS Biol* **18**, e3000715 (2020).
5. Klein, S. *et al.* SARS-CoV-2 structure and replication characterized by in situ cryo-electron tomography. *Nat Commun* **11**, 5885 (2020).
6. Betzig, E. *et al.* Imaging intracellular fluorescent proteins at nanometer resolution. *Science* **313**, 1642-1645 (2006).
7. Rust, M.J., Bates, M. & Zhuang, X. Sub-diffraction-limit imaging by stochastic optical reconstruction microscopy (STORM). *Nat. Methods* **3**, 793-796 (2006).
8. Heilemann, M. *et al.* Subdiffraction-Resolution Fluorescence Imaging with Conventional Fluorescent Probes. *Angew. Chem. Int. Ed.* **47**, 6172-6176 (2008).
9. Klar, T.A., Jakobs, S., Dyba, M., Egner, A. & Hell, S.W. Fluorescence microscopy with diffraction resolution barrier broken by stimulated emission. *Proceedings of the National Academy of Sciences of the United States of America* **97**, 8206-8210 (2000).
10. Gustafsson, M.G.L. Surpassing the lateral resolution limit by a factor of two using structured illumination microscopy. *J. Microsc.* **198**, 82-87 (2000).
11. Xu, K., Zhong, G. & Zhuang, X. Actin, Spectrin, and Associated Proteins Form a Periodic Cytoskeletal Structure in Axons. *Science* **339**, 452-456 (2013).
12. Andronov, L., Ouararhni, K., Stoll, I., Klaholz, B.P. & Hamiche, A. CENP-A nucleosome clusters form rosette-like structures around HJURP during G1. *Nature Communications* **10**, 4436 (2019).
13. Reinhardt, S.C.M. *et al.* Ångström-resolution fluorescence microscopy. *Nature* **617**, 711-716 (2023).
14. Baddeley, D. & Bewersdorf, J. Biological Insight from Super-Resolution Microscopy: What We Can Learn from Localization-Based Images. *Annual Review of Biochemistry* **87**, 965-989 (2018).
15. Wang, J. *et al.* Multi-color super-resolution imaging to study human coronavirus RNA during cellular infection. *Cell Reports Methods* **2**, 100170 (2022).
16. Wolff, G. *et al.* A molecular pore spans the double membrane of the coronavirus replication organelle. *Science* **369**, 1395-1398 (2020).
17. Lee, J.Y. *et al.* Absolute quantitation of individual SARS-CoV-2 RNA molecules provides a new paradigm for infection dynamics and variant differences. *eLife* **11**, e74153 (2022).
18. Pepe, A., Pietropaoli, S., Vos, M., Barba-Spaeth, G. & Zurzolo, C. Tunneling nanotubes provide a route for SARS-CoV-2 spreading. *Science Advances* **8**, eabo0171 (2022).
19. Sherman, E. *et al.* Functional Nanoscale Organization of Signaling Molecules Downstream of the T Cell Antigen Receptor. *Immunity* **35**, 705-720 (2011).
20. Razvag, Y., Neve-Oz, Y., Sajman, J., Reches, M. & Sherman, E. Nanoscale kinetic segregation of TCR and CD45 in engaged microvilli facilitates early T cell activation. *Nature Communications* **9**, 732 (2018).

21. Sawicki, S.G. & Sawicki, D.L. Coronavirus minus-strand RNA synthesis and effect of cycloheximide on coronavirus RNA synthesis. *Journal of Virology* **57**, 328-334 (1986).
22. Hillen, H.S. *et al.* Structure of replicating SARS-CoV-2 polymerase. *Nature* **584**, 154-156 (2020).
23. Gao, Y. *et al.* Structure of the RNA-dependent RNA polymerase from COVID-19 virus. *Science* **368**, 779-782 (2020).
24. Ahn, D.-G., Choi, J.-K., Taylor, D.R. & Oh, J.-W. Biochemical characterization of a recombinant SARS coronavirus nsp12 RNA-dependent RNA polymerase capable of copying viral RNA templates. *Archives of Virology* **157**, 2095-2104 (2012).
25. Naydenova, K. *et al.* Structure of the SARS-CoV-2 RNA-dependent RNA polymerase in the presence of favipiravir-RTP. *Proceedings of the National Academy of Sciences* **118**, e2021946118 (2021).
26. Eymieux, S. *et al.* Ultrastructural modifications induced by SARS-CoV-2 in Vero cells: a kinetic analysis of viral factory formation, viral particle morphogenesis and virion release. *Cellular and Molecular Life Sciences* **78**, 3565-3576 (2021).
27. Cortese, M. *et al.* Integrative Imaging Reveals SARS-CoV-2-Induced Reshaping of Subcellular Morphologies. *Cell Host & Microbe* **28**, 853-866.e855 (2020).
28. Lang, S. *et al.* An Update on Sec61 Channel Functions, Mechanisms, and Related Diseases. *Front Physiol* **8**, 887 (2017).
29. Hsu, J.C.-C., Laurent-Rolle, M., Pawlak, J.B., Wilen, C.B. & Cresswell, P. Translational shutdown and evasion of the innate immune response by SARS-CoV-2 NSP14 protein. *Proceedings of the National Academy of Sciences* **118**, e2101161118 (2021).
30. Mönkemöller, V. *et al.* Imaging fenestrations in liver sinusoidal endothelial cells by optical localization microscopy. *Physical Chemistry Chemical Physics* **16**, 12576-12581 (2014).
31. Oudshoorn, D. *et al.* Expression and Cleavage of Middle East Respiratory Syndrome Coronavirus nsp3-4 Polyprotein Induce the Formation of Double-Membrane Vesicles That Mimic Those Associated with Coronaviral RNA Replication. *mBio* **8**, 10.1128/mbio.01658-01617 (2017).
32. Liv, Z. *et al.* SARS-CoV-2 nsp3-4 suffice to form a pore shaping replication organelles. *bioRxiv*, 2022.2010.2021.513196 (2022).
33. Han, Y.-S. *et al.* Papain-Like Protease 2 (PLP2) from Severe Acute Respiratory Syndrome Coronavirus (SARS-CoV): Expression, Purification, Characterization, and Inhibition. *Biochemistry* **44**, 10349-10359 (2005).
34. Shin, D. *et al.* Papain-like protease regulates SARS-CoV-2 viral spread and innate immunity. *Nature* **587**, 657-662 (2020).
35. Hartenian, E. *et al.* The molecular virology of coronaviruses. *J Biol Chem* **295**, 12910-12934 (2020).
36. V'Kovski, P., Kratzel, A., Steiner, S., Stalder, H. & Thiel, V. Coronavirus biology and replication: implications for SARS-CoV-2. *Nat Rev Microbiol* **19**, 155-170 (2021).
37. Baggen, J., Vanstreels, E., Jansen, S. & Daelemans, D. Cellular host factors for SARS-CoV-2 infection. *Nature Microbiology* **6**, 1219-1232 (2021).
38. Andronov, L., Genthial, R., Hentsch, D. & Klaholz, B.P. splitSMLM, a spectral demixing method for high-precision multi-color localization microscopy applied to nuclear pore complexes. *Communications Biology* **5**, 1100 (2022).
39. Storti, B. *et al.* A spatial multi-scale fluorescence microscopy toolbox discloses entry checkpoints of SARS-CoV-2 variants in Vero E6 cells. *Computational and Structural Biotechnology Journal* **19**, 6140-6156 (2021).
40. Scherer, K.M. *et al.* SARS-CoV-2 nucleocapsid protein adheres to replication organelles before viral assembly at the Golgi/ERGIC and lysosome-mediated egress. *Science Advances* **8**, eabl4895 (2022).
41. Cao, C. *et al.* The architecture of the SARS-CoV-2 RNA genome inside virion. *Nature Communications* **12**, 3917 (2021).

42. Lan, T.C.T. *et al.* Secondary structural ensembles of the SARS-CoV-2 RNA genome in infected cells. *Nature Communications* **13**, 1128 (2022).
43. Gopal, A., Zhou, Z.H., Knobler, C.M. & Gelbart, W.M. Visualizing large RNA molecules in solution. *RNA* **18**, 284-299 (2012).
44. Schonborn, J. *et al.* Monoclonal antibodies to double-stranded RNA as probes of RNA structure in crude nucleic acid extracts. *Nucleic Acids Res* **19**, 2993-3000 (1991).
45. Ku, J. *et al.* Reactive Polymer Targeting dsRNA as Universal Virus Detection Platform with Enhanced Sensitivity. *Biomacromolecules* **21**, 2440-2454 (2020).
46. Deng, J. *et al.* SARS-CoV-2 NSP8 suppresses type I and III IFN responses by modulating the RIG-I/MDA5, TRIF, and STING signaling pathways. *Journal of Medical Virology* **95**, e28680 (2023).
47. Kumar, P. *et al.* The nonstructural protein 8 (nsp8) of the SARS coronavirus interacts with its ORF6 accessory protein. *Virology* **366**, 293-303 (2007).
48. Snijder, E.J. *et al.* Ultrastructure and origin of membrane vesicles associated with the severe acute respiratory syndrome coronavirus replication complex. *J Virol* **80**, 5927-5940 (2006).
49. Stertz, S. *et al.* The intracellular sites of early replication and budding of SARS-coronavirus. *Virology* **361**, 304-315 (2007).
50. Ulasli, M., Verheije, M.H., de Haan, C.A.M. & Reggiori, F. Qualitative and quantitative ultrastructural analysis of the membrane rearrangements induced by coronavirus. *Cellular Microbiology* **12**, 844-861 (2010).
51. Chiem, K., Ye, C. & Martinez-Sobrido, L. Generation of Recombinant SARS-CoV-2 Using a Bacterial Artificial Chromosome. *Current Protocols in Microbiology* **59**, e126 (2020).
52. Ye, C. *et al.* Rescue of SARS-CoV-2 from a Single Bacterial Artificial Chromosome. *mBio* **11**, 10.1128/mbio.02168-02120 (2020).
53. Schindelin, J. *et al.* Fiji: an open-source platform for biological-image analysis. *Nature methods* **9**, 676-682 (2012).
54. Barentine, A.E.S. *et al.* An integrated platform for high-throughput nanoscopy. *Nature Biotechnology* (2023).
55. Ovesny, M., Krizek, P., Borkovec, J., Svindrych, Z. & Hagen, G.M. ThunderSTORM: a comprehensive ImageJ plug-in for PALM and STORM data analysis and super-resolution imaging. *Bioinformatics (Oxford, England)* **30**, 2389-2390 (2014).
56. Schwarz, G. Estimating the dimension of a model. *The annals of statistics* **6**, 461-464 (1978).
57. Marin, Z. *et al.* PYMEVisualize: an open-source tool for exploring 3D super-resolution data. *Nature Methods* **18**, 582-584 (2021).
58. Pedregosa, F. *et al.* Scikit-learn: Machine Learning in Python. *J. Mach. Learn. Res.* **12**, 2825–2830 (2011).